Hindawi
Advances in Astronomy
Volume 2019, Article ID 3940837, 10 pages
https://doi.org/10.1155/2019/3940837

Research Article

Study of Chang'E-2 Microwave Radiometer Data in the Lunar Polar Region

Fan Yang, Yi Xu, Kwing Lam Chan, Xiaoping Zhang, Guoping Hu, and Yong Li

State Key Laboratory of Lunar and Planetary Sciences, Macau University of Science and Technology, Macau 999078, China

Correspondence should be addressed to Yi Xu; yixu@must.edu.mo

Received 5 February 2019; Accepted 7 April 2019; Published 24 April 2019

Guest Editor: Jing Li

The Chang'E-2 (CE-2) four-channel microwave radiometer (MRM) data with frequencies of 3 GHz, 7.8 GHz, 19.35 GHz, and 37 GHz have been used to investigate the properties of lunar surface such as regolith thickness, dielectric constant, and titanium abundance within a depth of several meters in middle and low latitudes. The purpose of this work is to take a close look at MRM data in the polar regions of the Moon and analyze the characteristics of the brightness temperature (TB) in permanently shadowed regions (PSRs), especially where evidence of water ice has been found. First, the comparisons of brightness temperature values in the polar region and in low latitudes show that (1) the periodic diurnal (day/night) variation of TB becomes weak in high latitudes since topography plays a dominant role in determining TB in polar region and (2) seasonal effects are more recognizable in polar region than in low latitudes due to the weak illumination condition. Second, even without direct sun illumination, significant seasonal variations of TBs are observed in PSRs, probably caused by the scattering flux from neighboring topography. TB Ratio (TBR) between channel 1 and channel 4, which indicates the differences of TB at different depths of lunar regolith, is higher and shows stronger seasonal variation in PSR than regions with direct illumination. Third, overall the distribution of high TBR values is in consistence with the water ice distributions obtained by the Moon Mineralogy Mapper instrument, the LAMP UV spectra, and the Lunar Prospector Neutron Spectrometer. The proportion of the summation over area with water ice proof in the regions of interest is 0.89 and 0.56 in south pole and north pole, respectively. The causes of the correlation of high TBR between different microwave frequencies and stability of water ice deposits still require further investigation, but MRM data shows unique characteristic in PSRs and could provide important information about the upper few meters of lunar regolith.

1. Introduction

Since Selene, Chang'E, Chandrayaan-1, and Lunar Reconnaissance Orbiter have fulfilled their missions successfully, more and more questions about the Moon appear. Whether the water ice exists in the lunar polar region is an essential one among these problems since it has both important scientific significance and potential application value as an important resource for human beings in the future lunar explorations.

Watson et al. firstly put forward the idea of the possible existence of the water ice in the permanently shadowed regions (PSRs) on the Moon because of the small obliquity and the large variation in topographic relief near the poles [1]. However, Stacy et al. and Campbell et al. did not find any evidence of water ice deposits in the lunar southern polar region, using the ground-based radar system to image the polar region [2, 3]. Nozette et al. found the presence of water ice after analyzing the Clementine bistatic radar data [4], but a reanalysis showed that radar data were not well-documented to demonstrate the existence of the water ice [5]. With the Miniature Radio Frequency (Mini-RF) radar data, Spudis discovered a different class of polar crater that exhibits high circular polarization ratio (CPR) which may associate with the presence of water ice [6]. However, Fa et al. found that the enhanced CPR is probably caused by rocks rather than ice deposits [7].

Analysis result from the Lunar Prospector (LP) neutron spectrometer indicated abundant hydrogen, which cannot be identified as water ice or other hydrogenated compounds, existing in PSRs [8, 9]. In 2009, water was detected after

the spacecraft of the Lunar Crater Observation and Sensing Satellite (LCROSS) impacted the Cabeus crater [10]. In addition, Hayne et al. had shown the location of the anomalous ultraviolet (UV) albedo consistent with water ice in the southern polar region, based on the Lyman Alpha Mapping Project (LAMP) UV spectra [11]. Recently, Li found the direct evidence of the surface exposed water ice in the lunar polar region with the Moon Mineralogy Mapper (M^3) instrument on the Chandrayaan-1 spacecraft [12].

Compared to infrared radiation, microwave signals originate from deeper layers and can reveal the physical properties of lunar regolith [13]. The microwave observation of the Moon started in 1946 [14, 15]. Then in Apollo era, a series of microwave ground-based observations of the Moon was made to obtain the physical parameters of the lunar surface by simulating the brightness temperature (TB) with theoretical models [16–22].

Lunar orbiters Chang'E-1 (CE-1) and Chang'E-2 (CE-2) were launched in 2007 and 2010, respectively. Both carried Microwave radiometer (MRM), which conducted passive microwave remote sensing measurements to obtain the TB of the lunar surface at 3, 7.8, 19.35, and 37 GHz (10, 3.84, 1.55, and 0.81 cm wavelengths) [23]. The first microwave map of the complete Moon was made by the CE-1 MRM data [24]. In polar region, CE-1 TB map shows some cold patches, where local temperature minima are independent of day and night due to absence of direct illumination in PSRs [13]. MRM data have also been utilized in inferring the properties of the upper few meters of lunar surface in low and middle latitudes; e.g., the thickness distribution of regolith was retrieved using the MRM data [25], the effective complex dielectric constant of lunar regolith as a function of the depth at different frequency channels [26], lunar (FeO + TiO_2) abundance [27], rock abundance, and others [28]. Also, people had studied basaltic volcanism of the Moon with MRM data [29].

The purpose of this work is to take a close look at MRM data in the polar regions of the Moon and analyze the characteristics of the TB in permanently shadowed regions, especially where plausible evidence of water ice has been found.

2. Chang'E TB Data

CE-2 observation covered the entire Moon by seven times and the local time coverage of the CE-2 data was over a complete lunation [30]. The total effective time of MRM data is 279818 min for 2401 tracks. The spatial resolutions of CE-2 MRM are 25 km and 17.5 km for 3 GHz and three remaining channels, respectively [31]. The absolute temperature accuracy is less than 0.5 K over the temperature range 100–350 K [30].

Note that MRM data have almost constant negative biases from theoretical results probably due to the heat contamination of cold reference antenna, but the variation trend of TB is still available [32, 33]. The microwave TB range is set as 30K-400K TB and points outside this range are considered as anomalous and excluded from this study [30]. Also, about ~0.92% of the total tracks were removed due to visible errors. Approximately 8,506,115 measurement points were selected in this work.

3. Data Comparisons and Analysis

3.1. TB in Low Latitude and High Latitude. The TB differences are more significant between channel 1 and channel 4 comparing with the other two channels. In addition, TB data of channel 2 contains a certain deviation from previous studies [32]. Therefore, we extract the TB data of channel 1 (3 GHz) and channel 4 (37 GHz) in the latitude zones 20° N/S, 80° N/S, and 85° N/S to analyze the changes of TB data during the whole observation mission. The width of the zones was ± 0.1° in latitude. The observation date varies from Oct. 15, 2010, to May 20, 2011. We analyze the TB in the daytime (6:00-18:00) and nighttime (0:00-6:00; 18:00-24:00) in the latitude zones 20° N/S. Here, the "hour angle" is used to define the lunar local time by Chan and Zheng [13, 24]. It is calculated from the solar incidence angle, the azimuth angle, and the latitude. The "hour angle" is converted into the "24-hour clock" local time.

The TB data at different latitude and their corresponding local time are shown in Figures 1(a)–1(g). In Figures 1(a)–1(d), we could observe, in low latitude, the changes of TB of channel 4 and channel 1 that are dominated by diurnal variation with lunar local time, although the diurnal variation of channel 1 is smaller than that of channel 4. Because channel 1 signal originates in deeper subsurface layer than channel 4, it is less sensitive to the sunlight and more stable during the lunation period. The effects of topography and physical properties of regolith also cause the vibrations of TB at the same local time, but they are masked by the effects of solar incidence. To extract the physical characteristics of lunar regolith or topography effects, the diurnal variation should be removed, e.g., with spherical harmonics fitting as proposed in [13, 30]. The TB of channel 4 between February and March in daytime is lower than that in nighttime mainly because of the fact that TB in the early morning is lower than that after dusk according to the result by Zheng [30]. The lunar local time of the data observed between February and March is almost around early morning (6:00 am to 8:00 am) and dusk (18:00 pm to 20:00 pm).

In Figures 1(a)–1(d), we also observe that the difference between latitudes 20° N and 20° S is within the range of 5% and the seasonal variations can be barely seen. It can be simply explained by the small obliquity of the Moon and the geographic symmetry. The illumination condition is almost the same between the southern and northern hemispheres in the low latitude area.

When latitude reaches 80° N/S, the ranges of TB diurnal variations largely reduce and are almost the same between channel 1 and channel 4 because of the decreasing solar illumination, as shown in Figure 1(e). TB variations caused by topography and other factors are similar to or even larger than diurnal variation. In high latitude, previously proposed spherical harmonics fitting method has limitations to fit TB variation curves and offset the changes of solar illumination and extract lunar regolith properties [13, 30]. Influences of topographic relief, scattering, and infrared radiation from

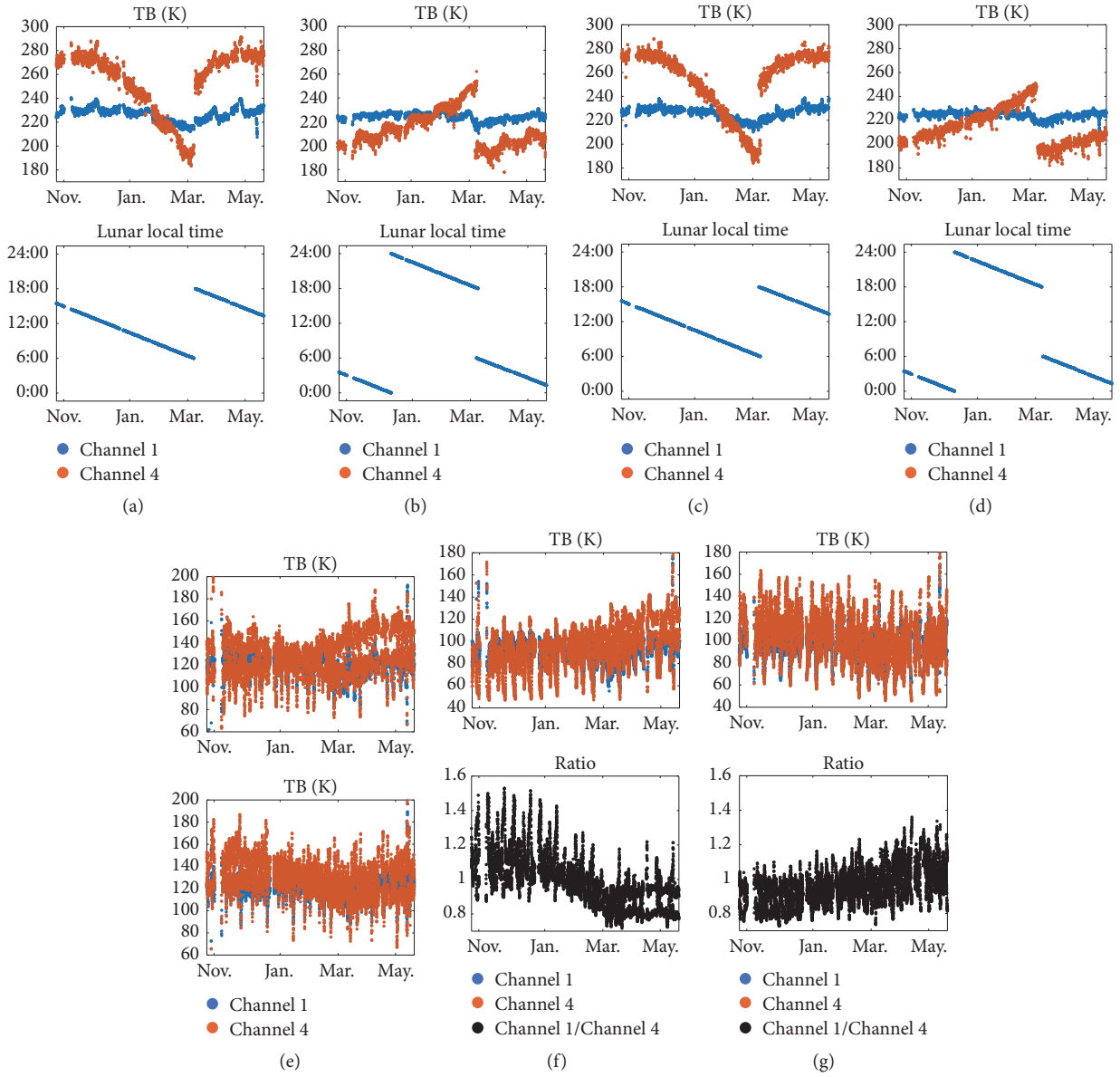

Figure 1: The data shown in (a)–(g) is selected in the latitude zones 20° N/S, 80° N/S, and 85° N/S, respectively. The upper part of (a)–(d) represents the fact that the TB of channel 1 and channel 4 varies during the whole observation period in daytime and nighttime at latitude 20° N ((a); (b)) and 20° S ((c); (d)), respectively. The bottom part of (a)–(d) shows the changes of lunar local time converted from "hour angle" of the corresponding TB data. Lunar local time varies with date nearly uniformly, so data diagram represents the TB variations in a half lunation cycle. The data shown in (e) represents the TB variations of channel 1 and channel 4 at 80° N and 80° S from top to bottom. The variations of TB and TB ratio between channel 1 and channel 4 are shown in (f) and (g) at 85° N (f) and 85° S (g) from top to bottom.

distant interior sunlit crater walls, etc., should be considered [34]. The trends of the TB variations in 80° N and 80° S are still almost the same, just like that in the low latitude.

The upper part in Figures 1(f) and 1(g) shows the TB variations at latitudes 85° N and 85° S, and the under part shows the TB Ration (TBR) variations between channel 1 and channel 4. Compared to low latitude area, the daytime and nighttime TB data in 85° N/S are less distinguished.

In addition, TB and TBR variations in 85° N and 85° S show opposite trends, especially the TBR. The TB increases slowly with the date in the north and decreases slowly in the south as shown in Figures 1(f) and 1(g). The reason for the difference can be explained by the seasonal variations. The seasonal variations of TB in high latitude are recognizable because the seasonal changes of solar flux become comparable to the day and night variations in high latitude, while diurnal variation of solar flux dominates in low latitude regions.

The lunar solar flux on flat surface at different latitude from Oct 15, 2010 (start time of Chang'E-2 MRM data) to Oct 15, 2011, was obtained from the ephemeris as shown in Figure 2. We use the SPICE toolkit [35] with the geometry of

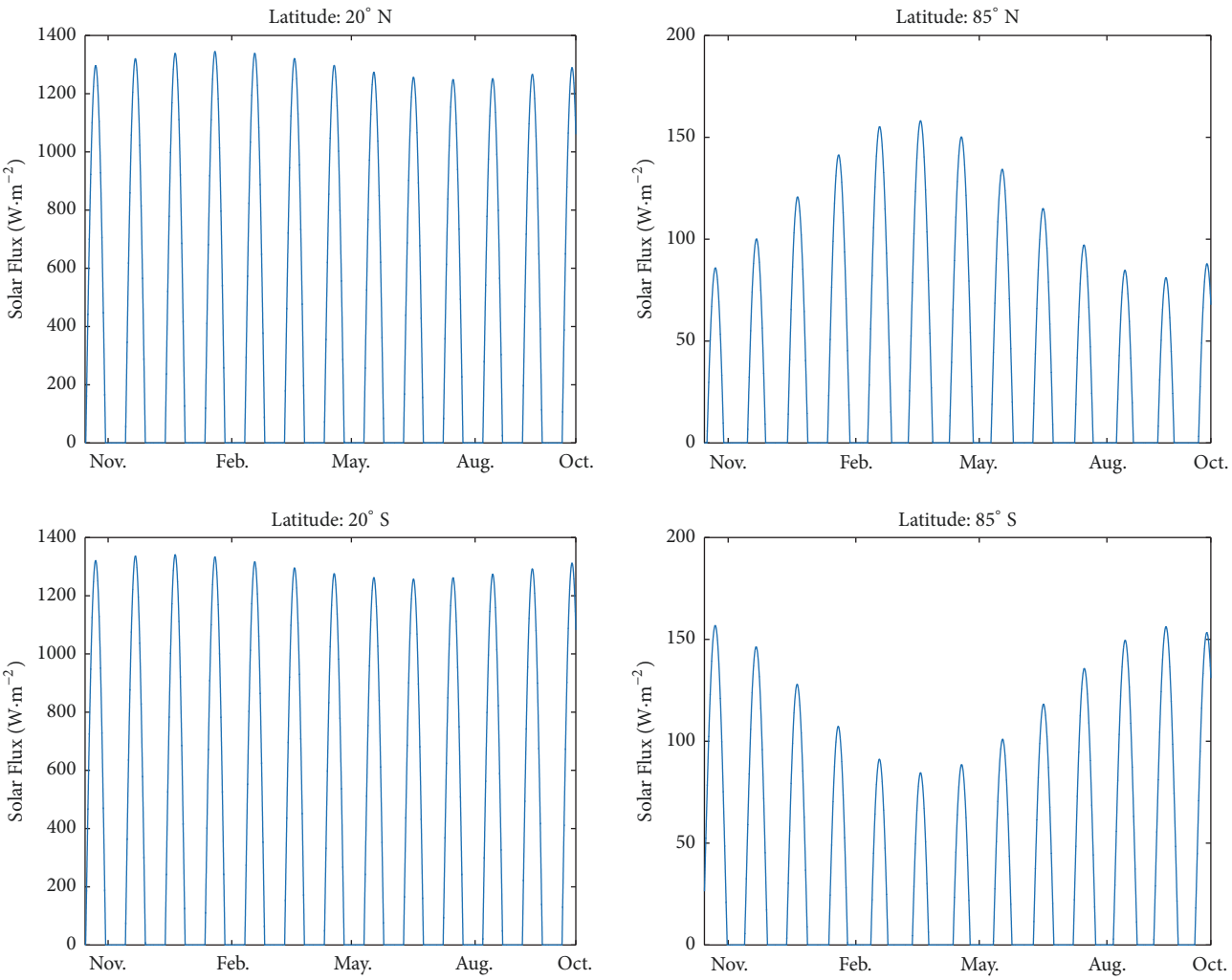

Figure 2: The solar flux varies from Oct 15, 2010 (start time of Chang'E-2 MRM data) to Oct 15, 2011, at latitudes ±20° and ±85°.

the Sun obtained from DE421 ephemeris [36] to generate the solar illumination data. The monthly maximum lunar solar flux varies from 158.1 W·m^{-2} to 81.1W·m^{-2} at the latitude 85° N and from 156.8 W·m^{-2} to 84.5 W·m^{-2} at 85° S; the value varies from 1345.3 W·m^{-2} to 1248.2 W·m^{-2} at the latitude 20° N and from 1340.8 W·m^{-2} to 1257.3 W·m^{-2} at 20° S. The relative change of monthly maximum lunar solar flux is larger at high latitude comparing with that in low latitude. This leads to the significant seasonal variations in high latitude and diurnal variation is more recognizable in low latitude.

3.2. TB in PSRs and Non-PSRs of Polar Regions. Figure 3(a) shows the TB and TBR in one of PSRs, Haworth Crater (-1.3° E, 87.5° S), and the Non-PSR regions (150° E, 87.5° S) in the same latitude, marked by the two green circles in the upper part of Figure 3(a). Figure 3(b) provides another comparison between PSR Amundsen Crater (92.3° E, 83.7° S) and the Non-PSR region (105° E, 83.7° S) in the same latitude. The center latitude and longitude of footprint of microwave radiometer are selected within 0.25° to reduce contamination from Non-PSR regions.

The time coverage of the MRM data in observation region is not enough to show clear diurnal variation. As shown in Figures 3(a) and 3(b), the range of TB variations of channels 1 and 4 in PSRs is not smaller than that in non-PSRs, although PSRs do not receive direct sun illumination and channel 1 TB is less sensitive to sun light than channel 4 TB due to different skin depth. It means that the scattering flux and thermal radiation play an important role in determining TB in PSR. Another difference between PSRs and Non-PSRs is the changes of TBR. The TBR increases rapidly with date in PSRs while that almost stays the same in Non-PSRs. The PSRs show an obvious seasonal variation. The maximum TBR during the observation period in PSR is higher than those in non-PSRs in the same latitude. Other comparisons between PSRs and non-PSRs show similar results.

Although PSRs do not receive direct sun light, they are still illuminated by the scattering flux and thermal radiations from neighboring topography [34, 37], which have seasonal variations at high latitude as shown in Figure 2. In addition, the solar flux in PSR is much weaker than that in Non-PSR due to topography relief, leading to much lower TB which

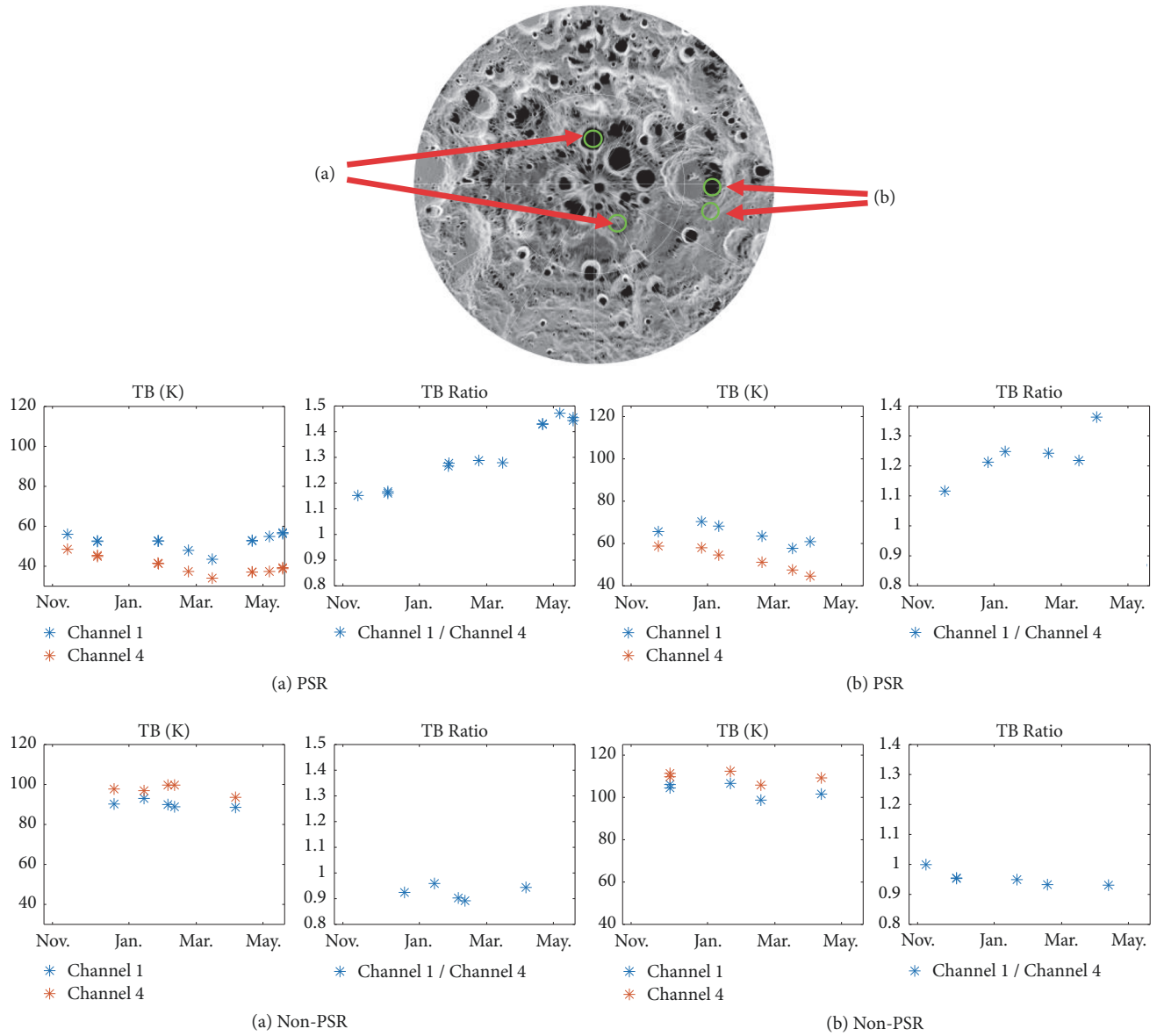

Figure 3: TB and TBR variations in Haworth Crater (PSR crater: -1.3° E, 87.5° S) and Non-PSR crater (150° E, 87.5° S) in the same latitude of Polar Regions; (b): TB and TBR variations in Amundsen Crater (PSR crater: 92.3° E, 83.7° S) and Non-PSR crater (105° E, 83.7° S) in the same latitude. The data is selected during the whole observation period. The green circles in the base map show the regions we selected. The base map is the Diviner annual maximum temperature map that varies from 30 K (black) to 345 K (white) in the Polar Regions (https://ode.rsl.wustl.edu/moon/indexDatasets.aspx).

is more sensitive to fluctuation of solar flux. Furthermore, although we select PSR with relatively large area to study characteristics of TB, the contamination of Non-PSR is unavoidable due to the large size of the footprint of the CE-2 microwave radiometer, which also contributed to the seasonal variations of TB in PSR. TB in channel 4 shows significant seasonal variations while TB in channel 1 is relative stable due to different penetration depth. Therefore, TBR between channel 1 and channel 4 also shows significant seasonal variations.

3.3. TB in PSR with Plausible Ice Evidence and Other PSRs. We analyzed the TB and TBR data in PSRs with plausible ice evidence and other PSRs in this section. Except for two large PSR craters mentioned in the previous section, here we select other three large PSR craters with plausible ice evidence and one large PSR crater without water ice observation at present [11, 12], considering the area of the PSR craters and the spatial resolution of CE-2 MRM data [37]. The red dots in the base map present the water ice distribution in the polar regions constrained by M^3, LOLA, and Diviner [12]. In Figure 4, the green circle in the base map shows the regions we selected.

Even TB values are lower than 100 K in all the observation regions, and TBR of those with plausible water ice could reach some high value such as 1.35, while the TBR varies from about 0.95 to 1.1 in Idel son L Crater, PSR crater without the plausible

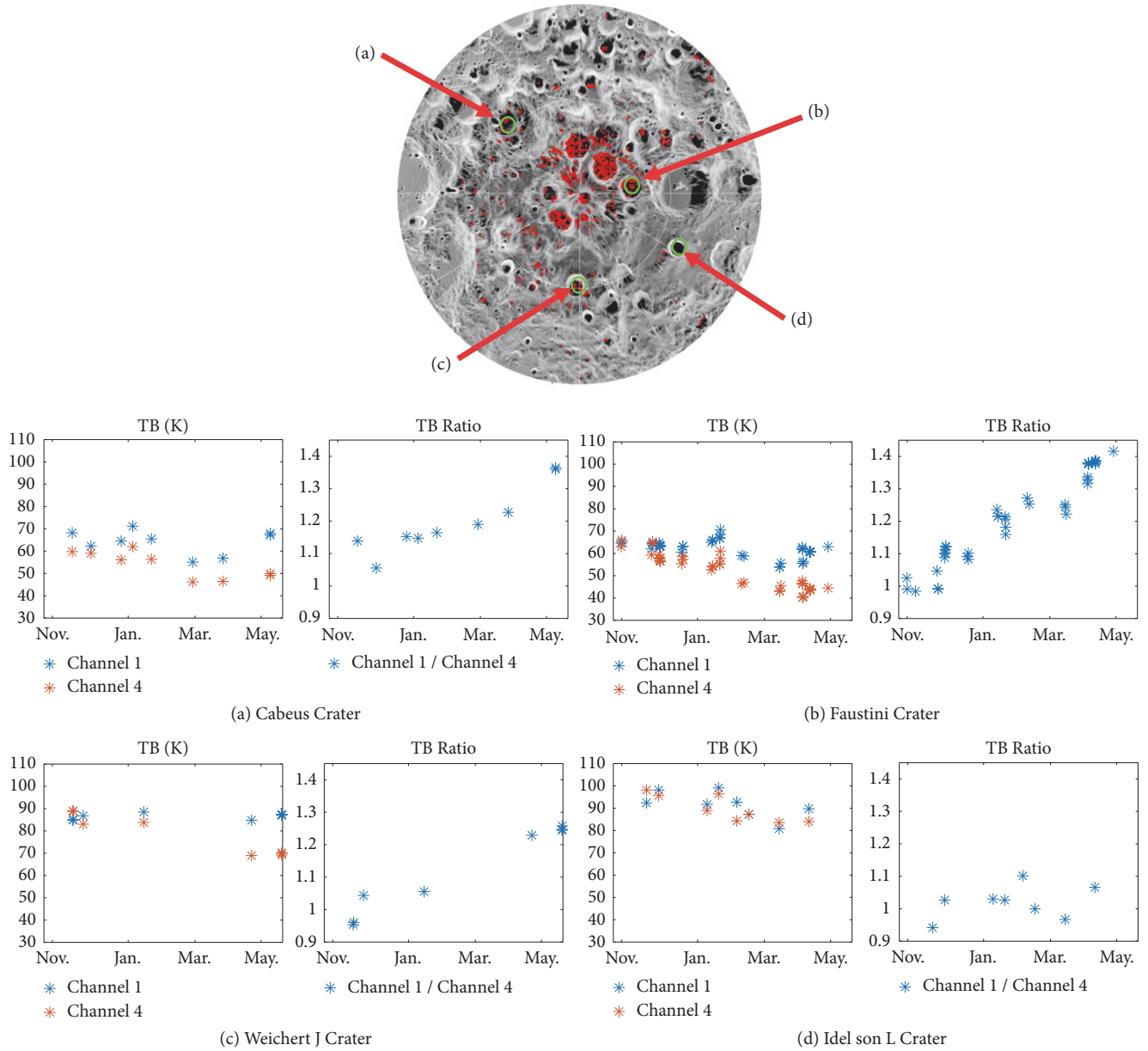

Figure 4: The TB and TBR variations during the whole observation period in (a) Cabeus Crater, (b) Faustini Crater, (c) Weichert J Crater, and (d) Idel son L Crater. The base map is the Diviner annual maximum temperature map that varies from 30 K (black) to 345 K (white) in the Polar Regions (https://ode.rsl.wustl.edu/moon/indexDatasets.aspx). The red dots in the base map present the water ice distribution in the polar regions constrained by M^3, LOLA, and Diviner [12]. The green circle in the base map shows the regions we selected.

ice evidence. The TBR reflects the TB differences between channel 1 and channel 4. Microwave signals in channel 1 and channel 4 originate from several meters and several centimeters depth of the lunar regolith, respectively. We could observe that high TBR resulted by relatively stable channel 1 TB and low channel 4 TB, which is easily affected by direct or indirect solar illumination and decreases with largely reduced solar flux in PSRs.

After measuring TBR of MRM data within 80° latitudes, the maximum value is below 1.35, which is selected as a threshold to generate high TBR distribution map as shown in Figures 5(a) and 5(b) to analyze if there is any correlation between the high TBR value distribution and water ice distribution constrained by other remote sensing data in the polar regions.

Figure 5 shows high MRM ratio value distribution maps, comparing with result using M^3 data by Li et al. [12]. In addition, Hayne et al. also found a high value of the off/on albedo ratio in Haworth crater and Faustini crater using the LAMP datasets, and the high value of the ratio represents the existence of the water ice [11]. Elphic et al. discovered high concentration of hydrogen in Haworth crater, Shoemaker crater, and Faustini crater using the LP neutron spectrometer data [38]. These craters are all PSR craters and they are

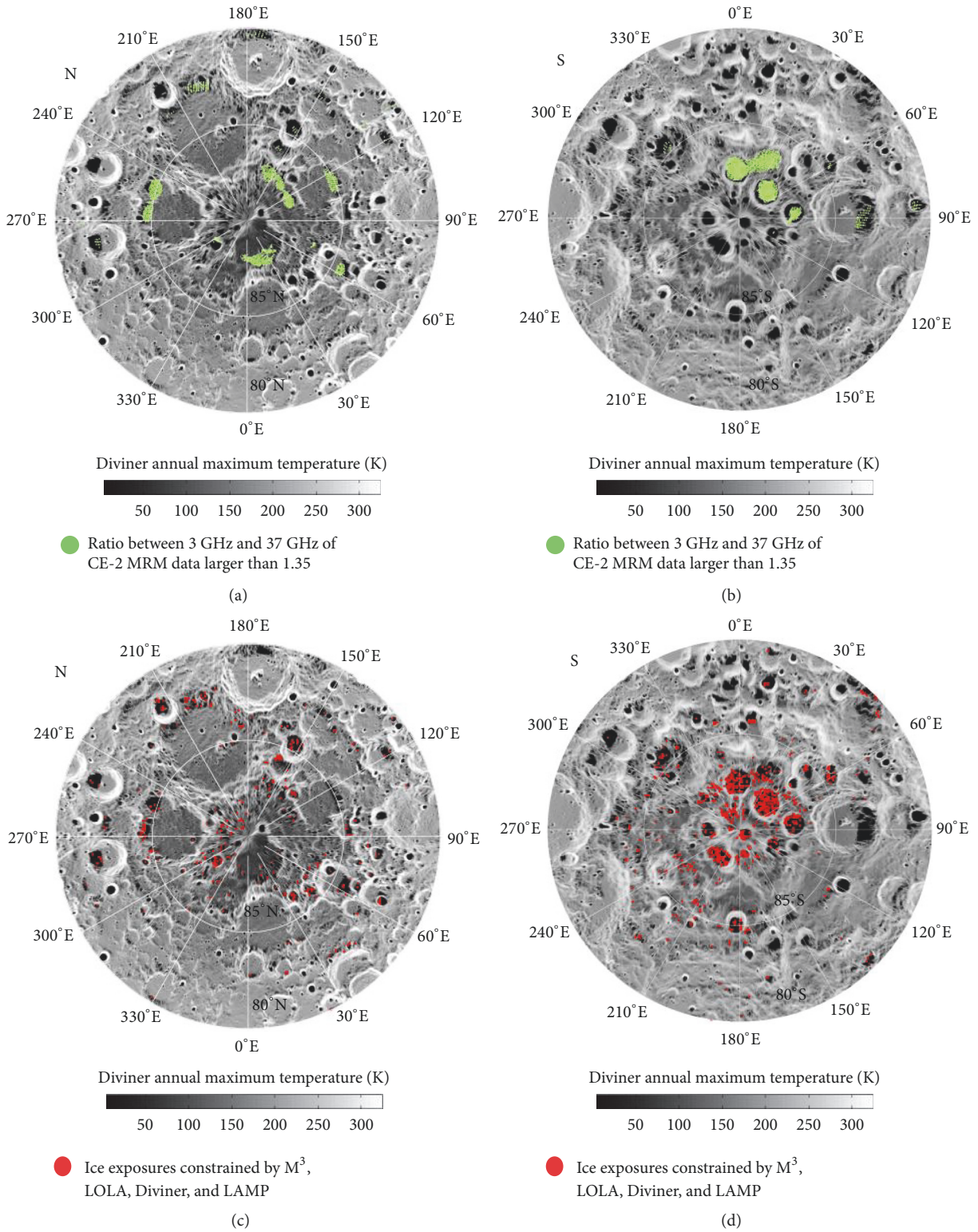

Figure 5: ((a) and (b)) Distribution of the ratio scattering points where it is no less than 1.35 overlain on the Diviner annual maximum temperature for the northern (a) and southern (b) polar regions; ((c) and (d)) Distribution of the water-ice-bearing pixels constrained by M^3, LOLA, and Diviner, overlain on the Diviner annual maximum temperature for the northern (c) and southern (d) polar regions [12].

potential places where water ice might exist. As we can see from Figure 5, the result using CE-2 MRM data has a good consistence with other instruments data to some extent.

The green dots indicating high TBR shown in Figures 5(a) and 5(b) are mainly concentrated in the dark areas where the temperature is lower than 100K, just like the results in (c) and (d), but not appearing in all the PSRs. Figures 5(a) and 5(c) show the distribution map in the northern polar region. Li gave an example in northern polar region where they got the direct evidence of the surface exposed water ice [12]. M^3 spectra data of Rozhdestvenskiy crater in the northern polar region implies that the surface exposed water ice could exist. The result of CE-2 MRM data in Rozhdestvenskiy crater also showed high ratio between 3 GHz and 37 GHz TB. There are some places that show different results. In Plaskett crater (180°E, 80°N), the top edge of Figures 5(a) and 5(c), no evidence from M^3 spectra data shows the existence of water ice, but CE-2 MRM data show high ratio there.

Figures 5(b) and 5(d) show the distribution maps in southern polar region. As we can see in the figure, high ratio of MRM (b) and the signature of water ice from M^3 all appear in the PSR areas. LAMP [11] and LP neutron spectrometer [38] showed the same results as well. For example, MRM data shows high TBR in the Cabeus crater (315°E, 84.5°S) where the water ice has been proved to be existing after the LCROSS impact experiment, so do the other three instruments which present the signature of water ice in this region. Some different results also appear among these data. LAMP shows low off/on albedo ratio in Shoemaker crater (48°E, 88°S) which means the low probability of the existence of the water ice. But high TBR of MRM and evidence of the water ice from M^3 and LP neutron spectrometer all present in this crater. High TBR of MRM and signature of water ice after analyzing data of LAMP and LP neutron spectrometer appear in the right part of Amundsen crater (90°E, 83.5°S), but the M^3 instrument shows different result. All the instruments present the signature of water ice in De Gerlache crater (270°E, 88.2°S) except that TBR value does not reach the threshold, which is 1.27.

To obtain the quantity value of the correlation between the water ice distribution retrieved from M^3 data [12] and distribution of TBR where it is no less than 1.35 in polar regions (80° N/S-90° N/S), we calculate the proportion of the summation over area with the M^3 data in the regions of interest for south pole and north pole, respectively.

The Chang'E-2 (TBR≥1.35) and M^3 data in the study area are collected in 15×15 km^2 bins. The boundaries of the disks in Figures 5(a)–5(d) are within the 80° latitude circle. The conditional correlation is defined as $C = N_{M^3 \cap CE-2}/N_{CE-2}$, N_{CE-2} which denotes the summation of the bins where TBR is no less than 1.35, and $N_{M^3 \cap CE-2}$ denotes the summation of the bins where TBR is no less than 1.35; M^3 data with water ice proof exists. The results are 0.74 and 0.56 in south and north poles, respectively. Amundsen crater is considered as place with water ice since evidence was provided by LP neutron spectrometer and LAMP, but M^3 data indicates that no water ice exists here. If we consider the Amundsen crater as the case with water ice, the results are 0.89 and 0.56 in south pole and north pole, respectively. Note that only the regions where the TBR is no less than 1.35, not the whole pole regions, are included in the calculation to minimize the impact of the "irrelevant" areas with no water ice. Therefore, high TBR regions are found to coincide well with the water ice deposits areas. For data validation, we use different bin sizes to calculate correlation between M^3 water ice results and our TBR data. Changing the bins into 25×25 km^2, the conditional correlation is 0.74 and 0.76 in south and north poles considering the Amundsen crater without water ice. The results still show high correlation between two sets of data, similar to results generated with 15×15 km^2 bins. The data and the correlation method are validated. The M^3 data that indicates that the water ice exists in the lunar polar region is given by Li [12].

One of the possibilities to explain the correlation between high TBR and water ice deposits could be the fact that water ice deposits are stable in the low temperature environment. Thus, we statistically study high TBR distribution and low TB distribution of channel 4. Based on statistic results, high maximum TBR (≥1.35) always appears in the places where TB of channel 4 is lower than 100 K, which also indicates low physical temperature. However, only 1.37% locations with low TB of channel 4 (< 100 K) can reach high maximum TBR. Hence, in addition to low temperature, obtaining high maximum TBR has other requirements such as the fact that area of PSR is larger than certain threshold, which is related with MRM data spatial resolution. Another scenario is that in regions with plausible water ice proof channel 4 TB usually is lower than channel 1 TB, which indicates low mobility of water molecules in these regions so that water molecules deposits will not diffuse below the surface and can be detected by remote sensing experiments at the surface of the Moon such as the imaging spectrometer M^3 [39]. Other speculations of such correlation include the fact that the presence of water ice deposits changes the average physical properties of lunar regolith, e.g., thermal inertia, dielectric constant, which results in large TB variations at different depths. Simulation of TB with physical parameters of lunar regolith and accurate solar flux in PSRs is necessary to provide proof for such speculation; however, the difficulty in obtaining the thermophysical parameters of lunar regolith at extreme low temperature and unknown rock abundance, etc., would result in the uncertainties of results [40]. Whether the temperature resolution of MRM data is enough to detect the presence of ice deposits is also questionable.

4. Conclusions

The comparisons of the TB variations in different latitudes show that the periodic diurnal variation of TB is dominant in the low latitude and becomes weak in the polar region. Second, in polar region, the topographical influences cause significant TB variations and seasonal effects are recognizable due to the weak illumination and the small obliquity of the Moon. Therefore, previous TB normalization method for latitude and local time is no longer suitable for polar regions. Third, even without the direct sun illumination, obvious seasonal variations of TBs are observed in PSRs,

probably caused by the scattering flux and thermal radiations from neighboring topography. Fourth, TBR between channel 1 and channel 4, which indicates TB variation at different depths of lunar regolith, shows stronger seasonal variation in PSR than others in the same latitude. Also, TBR in the PSRs with plausible water ice evidence could reach relatively high value. Overall, the distribution of high TBR is in good consistence with potential water ice distribution obtained by other types of equipment, e.g., LAMP, LP, and M^3. The areas with anomaly high value of TBR mainly appear in PSRs, such as Haworth crater, Shoemaker crater, Faustini crater, and Cabeus Crater where ice water most likely exists according to remote sensing data, but not vice versa.

The correlation between distribution of high TBR and plausible water ice proofs could be due to the low temperature environment indicated by high TBR. However, high TBR implies other conditions such as large PSR area. It also means that temperature of the surface is lower than that several meters deeper, which keeps water molecules on the surface instead of diffusing to the subsurface layers.

Data Availability

The data used to support the findings of this study are available from the corresponding author upon request.

Conflicts of Interest

The authors declare that they have no conflicts of interest.

Acknowledgments

This work is supported by Macao Science and Technology Development Fund in Macao Special Administrative Region: 0042/2018/A2 and 0089/2018/A3. The Chang'E data was supported by National Astronomical Observatories, Chinese Academy of Sciences. The authors would like to thank Li Shuai from University of Hawaii who provided the water ice distribution map generated with M^3 data. They also thank Dr. Xiongyao Li from Institute of Geochemistry of Chinese Academy of Sciences for the valuable comments and suggestions.

References

[1] K. Watson, B. C. Murray, and H. Brown, "The behavior of volatiles on the lunar surface," *Journal of Geophysical Research*, vol. 66, no. 9, pp. 3033–3045, 1961.

[2] N. J. S. Stacy, D. B. Campbell, and P. G. Ford, "Arecibo radar mapping of the lunar poles: a search for ice deposits," *Science*, vol. 276, no. 5318, pp. 1527–1530, 1997.

[3] D. B. Campbell, B. A. Campbell, L. M. Carter, J.-L. Margot, and N. J. S. Stacy, "No evidence for thick deposits of ice at the lunar south pole," *Nature*, vol. 443, no. 7113, pp. 835–837, 2006.

[4] S. Nozette, C. L. Lichtenberg, P. Spudis et al., "The Clementine bistatic radar experiment," *Science*, vol. 274, no. 5292, pp. 1495–1498, 1996.

[5] R. A. Simpson and G. L. Tyler, "Reanalysis of Clementine bistatic radar data from the lunar South Pole," *Journal of Geophysical Research: Planets*, vol. 104, no. E2, pp. 3845–3862, 1999.

[6] P. D. Spudis, D. B. J. Bussey, S. M. Baloga et al., "Evidence for water ice on the moon: results for anomalous polar craters from the LRO Mini-RF imaging radar," *Journal of Geophysical Research: Planets*, vol. 118, no. 10, pp. 2016–2029, 2013.

[7] W. Fa and Y. Cai, "Circular polarization ratio characteristics of impact craters from Mini-RF observations and implications for ice detection at the polar regions of the moon," *Journal of Geophysical Research: Planets*, vol. 118, no. 8, pp. 1582–1608, 2013.

[8] W. C. Feldman, S. Maurice, A. B. Binder, B. L. Barraclough, R. C. Elphic, and D. J. Lawrence, "Fluxes of fast and epithermal neutrons from lunar prospector: evidence for water ice at the lunar poles," *Science*, vol. 281, no. 5382, pp. 1496–1500, 1998.

[9] W. C. Feldman, D. J. Lawrence, R. C. Elphic et al., "Chemical information content of lunar thermal and epithermal neutrons," *Journal of Geophysical Research: Planets*, vol. 105, no. E8, pp. 20347–20363, 2000.

[10] A. Colaprete, P. Schultz, J. Heldmann et al., "Detection of water in the LCROSS ejecta plume," *Science*, vol. 330, no. 6003, pp. 463–468, 2010.

[11] P. O. Hayne, A. Hendrix, E. Sefton-Nash et al., "Evidence for exposed water ice in the Moon's south polar regions from Lunar Reconnaissance Orbiter ultraviolet albedo and temperature measurements," in *Proceedings of the Annual Meeting of the Lunar Exploration Analysis Group*, vol. 1820, Laurel, MD, USA, 2014.

[12] S. Li, P. G. Lucey, R. E. Milliken et al., "Direct evidence of surface exposed water ice in the lunar polar regions," *Proceedings of the National Acadamy of Sciences of the United States of America*, vol. 115, no. 36, pp. 8907–8912, 2018.

[13] K. L. Chan, K. T. Tsang, B. Kong, and Y.-C. Zheng, "Lunar regolith thermal behavior revealed by Chang'E-1 microwave brightness temperature data," *Earth and Planetary Science Letters*, vol. 295, no. 1-2, pp. 287–291, 2010.

[14] R. H. Dicke, "The measurement of thermal radiation at microwave frequencies," in *Classics in Radio Astronomy*, pp. 106–113, Springer, Dordrecht, Netherlands, 1946.

[15] R. H. Dicke and R. Beringer, "Microwave radiation from the sun and moon," in *Classics in Radio Astronomy*, pp. 218-219, Springer, Dordrecht, Netherlands, 1946.

[16] S. J. Keihm, "Effects of subsurface volume scattering on the lunar microwave brightness temperature spectrum," *Icarus*, vol. 52, no. 3, pp. 570–584, 1982.

[17] S. J. Keihm, "Interpretation of the lunar microwave brightness temperature spectrum: feasibility of orbital heat flow mapping," *Icarus*, vol. 60, no. 3, pp. 568–589, 1984.

[18] S. J. Keihm and M. G. Langseth, "Lunar microwave brightness temperature observations reevaluated in the light of Apollo program findings," *Icarus*, vol. 24, no. 2, pp. 211–230, 1975.

[19] S. J. Keihm and M. G. Langseth, "Microwave emission spectrum of the moon: mean global heat flow and average depth of the regolith," *Science*, vol. 187, no. 4171, pp. 64–66, 1975.

[20] S. J. Keihm and J. A. Cutts, "Vertical-structure effects on planetary microwave brightness temperature measurements: Applications to the lunar regolith," *Icarus*, vol. 48, no. 2, pp. 201–229, 1981.

[21] S. J. Keihm, K. Peters, M. G. Langseth, and J. L. Chute Jr., "Apollo 15 measurement of lunar surface brightness temperatures: thermal conductivity of the upper 1 1/2 meters of regolith," *Earth and Planetary Science Letters*, vol. 19, no. 3, pp. 337–351, 1973.

[22] D. D. Morabito, W. Imbriale, and S. Keihm, "Observing the moon at microwave frequencies using a large-diameter deep space network antenna," *IEEE Transactions on Antennas and Propagation*, vol. 56, no. 3, pp. 650–660, 2008.

[23] Y. Zheng, Z. Ouyang, C. Li, J. Liu, and Y. Zou, "China's lunar exploration program: present and future," *Planetary and Space Science*, vol. 56, no. 7, pp. 881–886, 2008.

[24] Y. Zheng, K. Tsang, K. Chan, Y. Zou, F. Zhang, and Z. Ouyang, "First microwave map of the Moon with Chang'E-1 data: the role of local time in global imaging," *Icarus*, vol. 219, no. 1, pp. 194–210, 2012.

[25] W. Fa and Y. Jin, "Analysis of microwave brightness temperature of lunar surface and inversion of regolith layer thickness: primary results of Chang-E 1 multi-channel radiometer observation," *Science in China Series F: Information Sciences*, vol. 53, no. 1, pp. 168–181, 2010.

[26] X. Gong, D. A. Paige, M. A. Siegler, and Y.-Q. Jin, "Inversion of dielectric properties of the lunar regolith media with temperature profiles using chang'e microwave radiometer observations," *IEEE Geoscience and Remote Sensing Letters*, vol. 12, no. 2, pp. 384–388, 2015.

[27] Z. Meng, G. Yang, J. Ping, Z. Cai, A. Gusev, and E. M. Osei, "Influence of (FeO+TiO2) abundance on the microwave thermal emissions of lunar regolith," *Science China Earth Sciences*, vol. 59, no. 7, pp. 1498–1507, 2016.

[28] R. Bugiolacchi, G. Hu, and K. L. Chan, "A new look at the Moon using Chang'e-2 microwave radiometer data," in *Proceedings of the European Planetary Science Congress*, vol. 12, Berlin, Germany, 2018.

[29] Z. Meng, S. Hu, T. Wang, C. Li, Z. Cai, and J. Ping, "Passive microwave probing mare basalts in mare imbrium using CE-2 CELMS data," *IEEE Journal of Selected Topics in Applied Earth Observations and Remote Sensing*, vol. 11, no. 9, pp. 3097–3104, 2018.

[30] Y. Zheng, K. L. Chan, K. T. Tsang et al., "Analysis of Chang'E-2 brightness temperature data and production of high spatial resolution microwave maps of the Moon," *Icarus*, vol. 319, pp. 627–644, 2019.

[31] Z. Z. Wang, Y. Li, X. H. Zhang et al., "Calibration and brightness temperature algorithm of CE-1 Lunar Microwave Sounder (CELMS)," *Science China Earth Sciences*, vol. 53, no. 9, pp. 1392–1406, 2010.

[32] G.-P. Hu, K. L. Chan, Y.-C. Zheng, K. T. Tsang, and A.-A. Xu, "Comparison and evaluation of the Chang'E microwave radiometer data based on theoretical computation of brightness temperatures at the Apollo 15 and 17 sites," *Icarus*, vol. 294, pp. 72–80, 2017.

[33] M. A. Siegler and J. Feng, "Microwave remote sensing of lunar subsurface temperatures: reconciling Chang'e MRM and LRO diviner," in *Proceedings of the Lunar and Planetary Science Conference*, vol. 48, The Woodlands, TX, USA, 2017.

[34] D. A. Paige, M. Siegler A, J. Zhang A et al., "Diviner lunar radiometer observations of cold traps in the Moons south polar region," *Science*, vol. 330, no. 6003, pp. 479–482, 2010.

[35] C. H. Acton Jr., "Ancillary data services of NASA's navigation and ancillary information facility," *Planetary and Space Science*, vol. 44, no. 1, pp. 65–70, 1996.

[36] J. G. Williams, "DE421 lunar orbit, physical librations, and surface coordinates," 2008, ftp://ssd.jpl.nasa.gov/pub/eph/planets/ioms/de421_Moon_coord_iom.pdf.

[37] E. Mazarico, G. A. Neumann, D. E. Smith, M. T. Zuber, and M. H. Torrence, "Illumination conditions of the lunar polar regions using LOLA topography," *Icarus*, vol. 211, no. 2, pp. 1066–1081, 2011.

[38] R. C. Elphic, V. R. Eke, L. F. A. Teodoro, D. J. Lawrence, and D. B. J. Bussey, "Models of the distribution and abundance of hydrogen at the lunar south pole," *Geophysical Research Letters*, vol. 34, no. 13, 2007.

[39] R. O. Green, C. Pieters, P. Mouroulis, and T. Koch, "The Moon Mineralogy Mapper (M3) imaging spectrometer for lunar science: instrument description, calibration, on-orbit measurements, science data calibration and on-orbit validation," *Journal of Geophysical Research: Planets*, vol. 116, no. E10, 2011.

[40] R. Woods-Robinson, M. A. Siegler, and D. A. Paige, "Developing a new thermophysical model for lunar regolith soil at low temperatures," in *Proceedings of the AGU Fall Meeting Abstracts*, San Francisco, Calif, USA, 2016.